ACSNANO

www.acsnano.org

Small to Large Polaron Behavior Induced by Controlled Interactions in Perovskite Quantum Dot Solids

Juno Kim,[#] Yuanze Xu,[#] David Bain, Mingxing Li, Mircea Cotlet, Qiuming Yu,* and Andrew J. Musser*

Cite This: *ACS Nano* 2023, 17, 23079−23093

Read Online

ACCESS | Metrics & More | Article Recommendations | Supporting Information

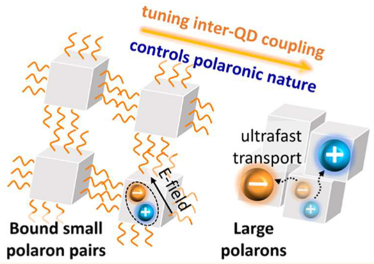

ABSTRACT: **The polaron is an essential photoexcitation that governs the unique optoelectronic properties of organic−inorganic hybrid halide perovskites, and it has been subject to extensive spectroscopic and theoretical investigation over the past decade. A crucial but underexplored question is how the nature of the photogenerated polarons is impacted by the microscopic perovskite structure and what functional properties this affects. To tackle this question, we chemically tuned the interactions between perovskite quantum dots (QDs) to rationally manipulate the polaron properties. Through a suite of time-resolved spectroscopies, we find that inter-QD interactions open an excited-state channel to form large polaron species, which exhibit enhanced spatial diffusion, slower hot polaron cooling, and a longer intrinsic lifetime. At the same time, polaronic excitons are formed in competition via localized band-edge states, exhibiting strong photoluminescence but are limited by shorter intrinsic lifetimes. This control of polaron type and function through tunable inter-QD interactions not only provides design principles for QD-based materials but also experimentally disentangles polaronic species in hybrid perovskite materials.**

KEYWORDS: *perovskite quantum dots, quantum dot interaction, ultrafast spectroscopy, polaron dynamics, polaron (de)localization*

INTRODUCTION

Organic−inorganic hybrid perovskites (OIHPs) have demonstrated promising potential in applications spanning photovoltaics,[1] light-emitting diodes,[2] X-ray detectors,[3] and lasers,[4] thanks to their superior optoelectronic properties.[5] Rational application of these materials must be underpinned by a detailed understanding of the nature and dynamics of the principal excitations and how they are connected to the material structure. In OIHPs, polarons are the essential photoexcitation that governs their unique optoelectronic properties, such as long (hot) carrier lifetime and moderate carrier mobility.[6,7] These are frequently discussed in terms of Fröhlich polarons, in which the charge carriers are dressed with nuclear polarization that arises via electron−phonon couplings and the ferroelectric properties of OIHPs.[8−13] Evidence of polaronic species in OIHPs spanning a wide range of dimensionalities and chemical compositions has been provided by time-resolved X-ray, electron diffraction, and terahertz spectroscopies which track time-dependent nuclear displacements during the polaron formation.[14−23] Complementary insights into the underlying electron−phonon couplings that drive polaron formation have been extracted from oscillatory components in the temporal profiles of pump−probe and multidimensional electronic spectroscopies.[24−34]

Despite their widespread observation, many questions remain about the detailed nature of the photogenerated polarons in OIHPs, including the role of functionally distinct small and large polarons and polaron pair states including bipolarons and polaronic excitons.[34−39] In parallel to this pursuit of fundamental photophysical understanding, various low-dimensional forms of OIHPs have been fabricated for practical photovoltaic applications, resulting in a library of materials with distinct characteristic microscopic structures.[40−43] A critical next step for the field is to develop a deeper understanding of how these different microstructures impact the nature and properties of photogenerated polarons. Delocalization, mobility, and interactions between polarons are crucial properties that should depend on microscopic structures and directly affect polaron dynamics,[44] but tackling these systematically remains a challenge.

Quantum dots (QDs) offer a promising platform to study polaron behaviors in OIHPs. The polaron behaviors in QDs can be rationally designed by controlling the interactions between the QDs for various applications. For example,

Received: September 13, 2023
Revised: November 1, 2023
Accepted: November 2, 2023
Published: November 7, 2023

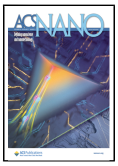

https://doi.org/10.1021/acsnano.3c08748
ACS Nano 2023, 17, 23079−23093

photovoltaic devices require a reduction in the dielectric barriers across QDs to facilitate charge dissociation and transport,[45] while in electroluminescent devices, the rational design of type I core−shell structures and surface passivation ligands both allows charge injection and maintains high radiative efficiency.[46] Similarly, by modulating the inter-QD distances and hence the electronic properties in QD solids, the properties of polarons in the OIHP can be revealed and tailored. Recent work on lead chalcogenide QD thin films—in which strong quantum confinement meant bound excitons were the primary excitation—exploited this approach to tunably induce ultrafast energy transport through control of QD spacing.[47]

In this work, we apply this concept to the polaron dynamics of formamidinium lead triiodide ($FAPbI_3$), one of the most widespread hybrid perovskite compositions where fundamental insights into the polaron behavior are needed to guide practical applications.[48−50] In the $FAPbI_3$ composition, the low exciton binding energy (∼20 meV) ensures that photoexcitations are efficiently converted to polarons at room temperature.[51] We prepare QDs with an average diameter of ∼13 nm, which is at the border of the exciton Bohr radius in this material.[52,53] We deposit these into thin films from which we can chemically remove the ligands in the solid phase. The result is two types of QD films with subtly different electronic structure. We detect clear hallmarks of polarons in both structures. Through detailed time-resolved spectroscopic measurements, we reveal how the interplay between tunable inter-QD coupling and excitation energy gates the formation of large polarons versus small polaronic excitons and, thus, significantly alters the polaron lifetime, diffusivity, and carrier cooling dynamics.

RESULTS AND DISCUSSION

Synthesis of $FAPbI_3$ QDs and Steady-State Spectroscopy. The $FAPbI_3$ QDs were synthesized according to our reported methods with slight modification,[54] yielding rectangular-shaped QDs with an average edge length of 13.05 ± 1.79 nm (Figure S1a). Solid-state $FAPbI_3$ QD films were prepared by spin coating high concentration QD solutions (∼60 mg/mL) onto substrates, which resulted in ∼70 nm thick films, consisting of roughly 5−6 layers of QDs. These films are hereafter termed Pristine QD. To better understand the interactions without our QD films, we employed transmission electron microscopy (TEM). We prepared TEM samples using a more dilute QD solution in order to achieve monolayer assembly, providing direct visualization of the edge-to-edge separation between adjacent QDs in the solid. As shown in Figure 1(a), the as-synthesized QDs tend to assemble along the edges due to facet-to-facet interactions. The average edge-to-edge distance was measured to be 2.49 ± 0.31 nm (Figure S1b). Since the as-synthesized QDs have mixed ligand shells of insulating oleate and oleylammonium, which impose high dielectric barriers for charge transport, the charge carriers can move only between adjacent QDs via tunneling. To reduce the dielectric barriers between QDs, Pristine QD films were dipped into methyl acetate (MeOAc) to remove the insulating organic ligands, and we refer to the resulting films as Coupled QD. Upon dipping into MeOAc, the ligands detach from the QD surfaces and dissolve into the solution, leaving partially bare QD surfaces. The resulting high surface energy drives adjacent QD facets to merge, as shown in Figure 1(a), creating direct charge transport channels and enhancing the electronic coupling between QDs.

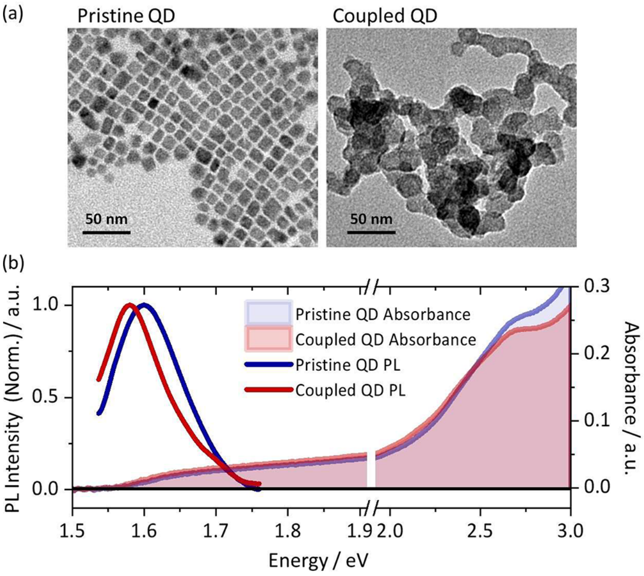

Figure 1. $FAPbI_3$ QD films. (a) Transmission electron microscopy (TEM) images of Pristine QD (left) and Coupled QD (right). (b) Steady-state absorption and PL spectra of Pristine QD (blue) and Coupled QD (red).

Figure 1(b) shows the steady-state absorption and photoluminescence (PL) spectra of Pristine QD and Coupled QD. To characterize the energy of band-edge states in the films, we plot the second derivative of their absorption spectra (Figure S2). Compared to Pristine QD, Coupled QD is red-shifted by 20 meV. The PL peak positions of both films are shifted similarly, resulting in nearly identical Stokes shift in both films. However, the PL line shape in Coupled QD following broadband white-light excitation (350−600 nm) is distinctly asymmetric, with a high-energy shoulder that points to the presence of multiple emissive species. Below, we use time-resolved PL measurements with tunable monochromatic excitation to reveal the different populations that contribute to the emission band. It is notable that the PL intensity is significantly lower in Coupled QD (Figure S3). The loss in the PL counts is due to the reduction of dielectric confinement after ligand removal and points to the different excitation decay pathways being available despite being based on similar QDs.

Femtosecond Transient Absorption Spectroscopy. To understand the impact of the induced electronic coupling between QDs, we investigated the electronic dynamics of both QD films with femtosecond transient absorption spectroscopy (fs-TA) as a function of pump photon energy and fluence (for details on the calculations of $<N_0>$, see Supplementary Note 1. $<N_0>$ refers to the average number of electron−hole pairs per QD upon photoexcitation). Three excitation wavelengths, 400, 520, and 780 nm, were selected, corresponding to $2xE_g$, $1.5xE_g$ and E_g, respectively. Representative TA spectra are shown in Figures 2, 3, 5 and Figures S4−S8.

Upon above-bandgap excitation (Figures 2 and S4−S7), the TA spectra of Pristine QD and Coupled QD manifest typical spectral features of $FAPbI_3$ and related compositions such as $MAPbI_3$ which we briefly review here.[55,56] The initial TA spectra ($\tau_{delay} < 0.3$ ps) show an asymmetric photobleaching (PB) band (1.6−2.0 eV) and a photoinduced absorption (PIA) band at slightly lower energies (∼1.55 eV). The asymmetric PB line shape arises from phase-space filling of hot polarons thermalized via carrier−carrier scattering (∼100 fs).[57]

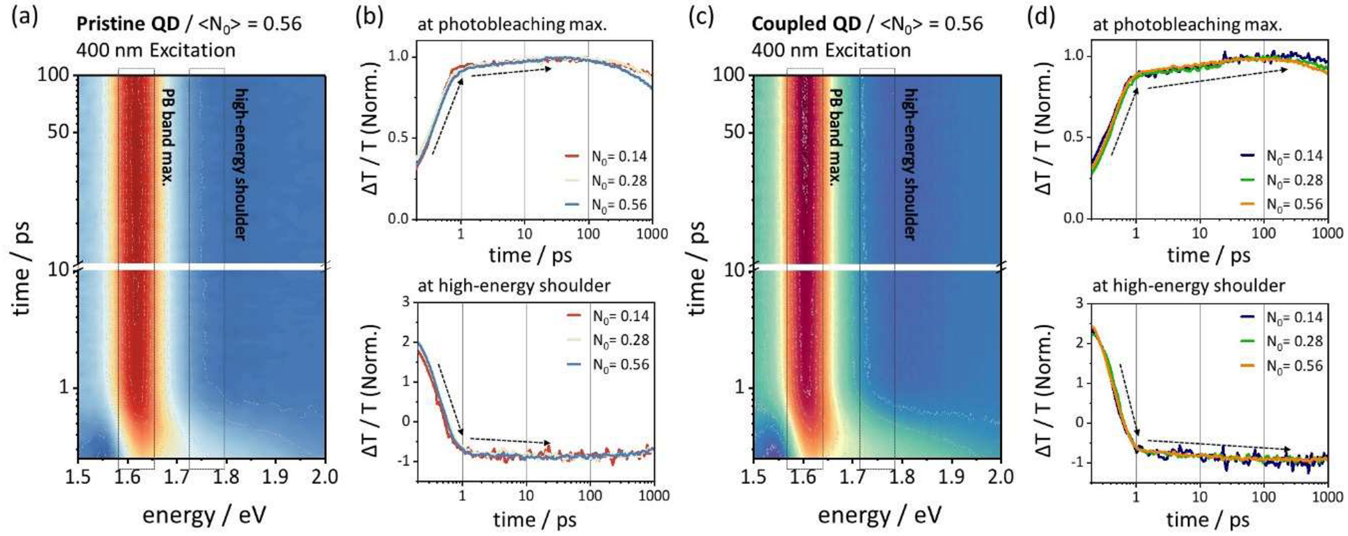

Figure 2. Polaron dynamics following 400 nm excitation. (a) fs-TA 2D contour map and (b) temporal profiles at the PB max and high energy PB shoulder region of Pristine QD. (c) fs-TA 2D contour map and (d) temporal profiles at the PB max and high energy PB shoulder region of Coupled QD. Excitation powers are indicated in terms of average number of photoexcitations per QD, <N_0>.

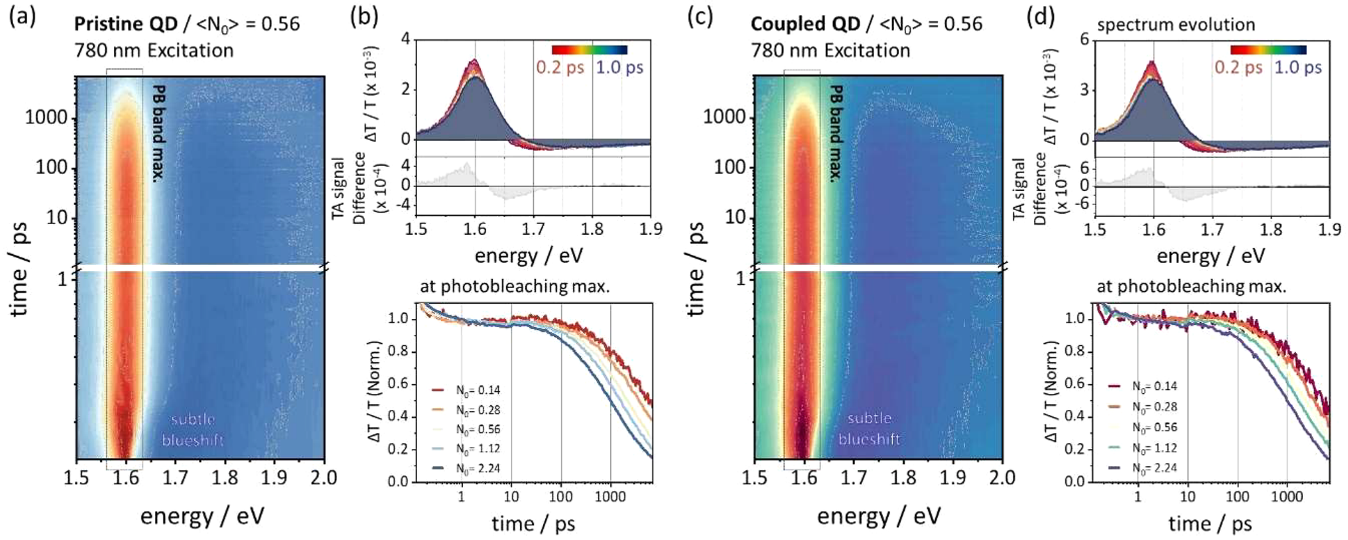

Figure 3. Polaron dynamics following band-edge 780 nm excitation. (a) fs-TA 2D contour map and (b) TA spectral evolution up to 1 ps (top) and temporal profiles at the PB max in the variance of pump fluence (bottom) of Pristine QD. (c) fs-TA 2D contour map and (d) TA spectral evolution up to 1 ps (top) and temporal profiles at the PB max in the variance of pump fluence (bottom) of Coupled QD. TA signal difference is obtained by subtracting TA spectrum at 0.2 ps from that at 1.0 ps. Excitation powers are indicated in terms of average number of photoexcitations per QD, <N_0>.

The low-energy PIA band has been attributed to bandgap renormalization (BGR).[58,59] By 1 ps delay, the hot polarons dissipate excess energy to the lattice and become thermally equilibrated with it.[60−63] During this cooling process, the PB band sharpens and gains intensity, while the BGR signature vanishes.[58] Beyond 1 ps, an additional PIA is evident at probe energies above 1.75 eV. This feature has been assigned to a range of effects, including photoinduced refractive index change and weak polaron PIA.[64] While these general features of $FAPbI_3$ are common to both films, we highlight that the PB band maximum in Coupled QD is red-shifted compared to that in Pristine QD, in accord with their static photoluminescence. Moreover, there are important differences between the films in the dynamics beyond the subpicosecond thermalization time scale (Figure 2(b),(d)), which we address in detail below.

First, we establish the baseline behavior of these materials using band-edge excitation (λ_{exc} = 780 nm, Figure 3). We find that Pristine QD and Coupled QD behave similarly under this condition. In the initial TA spectra, we observe no signature of the BGR PIA band, and the PB is sharp and intense due to the absence of hot polarons.[58] We also detect an ultrafast process (<0.5 ps) distinct from the thermalization above, during which the PB subtly blueshifts and decreases in intensity. With the assumption that the excited-state population remains constant on this ultrafast time scale, this change in spectral shape reflects a change in the nature of the excitations. Subtraction of the TA spectra before and after this process reveals an identical derivative line shape in both films (Figure 3(b),(d)). This basic behavior is maintained as a function of excitation density <N_0>, with the TA kinetics of Pristine QD and Coupled QD

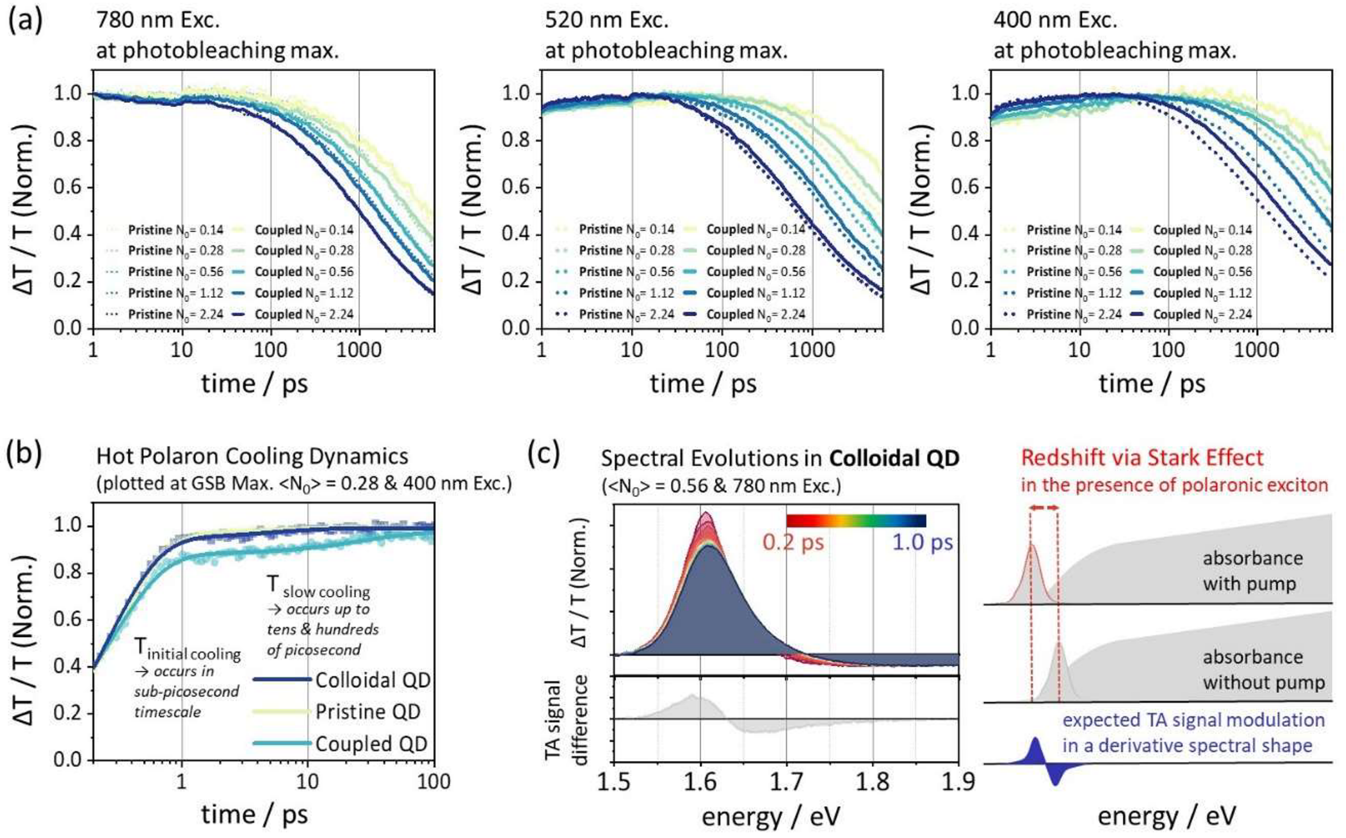

Figure 4. Pump-wavelength-dependent divergence in polaron dynamics. (a) Direct comparison of TA temporal profiles in the QD films upon 780, 520, and 400 nm excitations. (b) Direct comparison of hot polaron cooling dynamics in Colloidal QD, Pristine QD, and Coupled QD. (c) TA spectral evolution up to 1 ps upon 780 nm excitation in Colloidal QD (left) and expected TA signal modulation via the Stark Effect in the presence of polaronic exciton (right). TA signal difference is obtained by subtracting TA spectrum at 0.2 ps from that at 1.0 ps. Excitation power is indicated in terms of average number of photoexcitations per QD, <N_0>. All kinetics are extracted at the PB maximum.

nearly indistinguishable over the full measured fluence range (Figure 4(a)). A similar comparison for excitation at 520 and 400 nm reveals that the films diverge specifically under above-bandgap excitation, with Coupled QD yielding longer-lived polarons with distinctly slower cooling dynamics up to ∼300 ps (Figure 4(b)).

To disentangle the impact of interactions between QDs and the intrinsic processes within individual QDs, we further compare the fs-TA results on Colloidal QD (Figures 4(c), S8,S9). In the case of band-edge excitation (λ_{exc} = 780 nm), we capture the same fast spectral evolution seen in the films, resulting in derivative-like changes as shown in Figure 4(c). These fast spectral changes are independent of the coupling between QDs. We can rule out the possibility of surface traps as the origin of this effect due to the presence of native ligands at the surface of Colloidal QD. Indeed, equivalent experiments on Coupled QD passivated with FAI show identical behavior (Figure S10). The rapid evolution shown in Figures 3(b), 3(d), and 4(c) must thus reflect the same intrinsic, single-QD process in all three samples. These measurements cannot distinguish whether the dynamics occur within the QD core or are linked to the deformable lattice near the QD surface. Such effects should be constant across our samples, though, so the distinction is not significant for our analysis. Following above-bandgap excitation of Colloidal QD (λ_{exc} = 400 nm, Figures S8), these intrinsic effects are obscured on <1 ps time scales by the signatures of hot polaron generation and subsequent cooling. In the picosecond time scale, the temporal profile at low power (<N_0> = 0.14) shows an additional relaxation up to 30 ps. These colloidal polaron generation and cooling dynamics are in excellent agreement with those of Pristine QD (Figure 4(b)), indicating that this film is likewise dominated by single-QD processes. However, the carrier relaxation on intermediate time scales is distinctly slower in Coupled QD, lasting up to 300 ps. That is, the polaron dynamics become increasingly sensitive to inter-QD interactions upon above-bandgap excitation.

The distinction between single- and inter-QD processes is carried into the polaron recombination dynamics over a range of <N_0> values. Under band-edge conditions, Pristine QD and Coupled QD exhibit similar dynamics and no spectral evolution during recombination (Figures 3, 4(a), and S11). The dynamics can be well described with multiexponential kinetics, including the fast single-QD (τ_{PE}) process related to the derivative-like spectral evolution and a variable balance between monomolecular (τ_{mono}) and bimolecular ($\tau_{many\text{-}body}$) polaron recombination processes (Table 1). We obtain consistent values for the time constants $\tau_{many\text{-}body}$ and τ_{mono} over the full range of <N_0> explored: only the relative amplitudes of these channels change (Figure S15). The increase in the $\tau_{many\text{-}body}$ channel at higher powers links it to decay via a many-body process, while the corresponding decrease in τ_{mono} flags it as an intrinsic, geminate pathway.[65,66]

The recombination signatures following above-band gap excitation are more involved (Figures 5 and S6−S7). We show that Pristine QD exhibits a subtle redshift of the PB band

Table 1. Kinetic Parameters for Band-Edge Excitation Results[a]

	Pristine QD/780 nm exc.			Coupled QD/780 nm exc.		
	τ_{PE} (ps)	$\tau_{\text{many-body}}$ (ps)	τ_{mono} (ns)	τ_{PE} (ps)	$\tau_{\text{many-body}}$ (ps)	τ_{mono} (ns)
$<N_0>$ = 0.14	<0.2		5.5	<0.2		5.0
$<N_0>$ = 0.28	<0.2	520	5.5	<0.2	440	5.0
$<N_0>$ = 0.56	<0.2	510	5.5	<0.2	450	5.0
$<N_0>$ = 1.12	<0.2	560	5.5	<0.2	490	5.0
$<N_0>$ = 2.24	<0.2	540	5.5	<0.2	460	5.0

[a] Three time constants were obtained from fs-TA decay profiles. The rate constant of the fast single-QD process (τ_{PE}) is not precisely assigned by our time resolution of fs-TA. Monomolecular lifetime is fixed by the time constant obtained by ns-PL measurements.

during population decay, whereas the peak position is constant over time in Coupled QD. To better capture the spectral evolution, we again directly subtract (normalized) TA spectra at time delays chosen to exclude contributions from hot polaron cooling (Figures 5(c) and S16−S19). For Pristine QD, spectral subtraction once again shows a derivative line shape, albeit of opposite sign to that from the early time evolution in Figure 3(b). In contrast, the equivalent analysis of Coupled QD does not exhibit any such derivative but instead exhibits a small positive band at higher probe energy. The associated kinetics are fitted well by four exponents (Figures S12 and S13) representing biphasic carrier cooling dynamics and monomolecular and bimolecular recombination processes. The $\tau_{\text{many-body}}$ channel in Coupled QD shows a gradual reduction in lifetime and increased fitting weight with increasing $<N_0>$, pointing to many-body processes that are accelerated at high polaron density. The most notable differences between films are the systematically longer decay constants in Coupled QD, particularly the $<N_0>$-independent polaron lifetime τ_{mono} (Table 2).

Femtosecond Transient Absorption Spectroscopy at 140 K. The differences in spectral evolution and recombination dynamics between Pristine QD and Coupled QD suggest the presence of distinct photoexcited species in the two films. To verify their polaronic nature, we conducted fs-TA measurements at a low temperature (140 K), where clear oscillatory features in the kinetics (Figure S26) provide a direct signature of electron−phonon couplings. At this temperature, we observe the same phenomenology as a function of film type, pump fluence, and pump photon energy described above, including the derivative-like spectral shape changes on band-edge excitation and the detection of an additional slow carrier relaxation channel and enhanced τ_{mono} in Coupled QD following the above-gap excitation (Figures S20−S25). In short, we find no major alteration to the photophysical pathways at 140 K and consider this regime representative of the RT physics above.

We extracted the oscillatory component from the slowly varying electronic kinetics and performed the fast Fourier transform (FFT) at each probe energy. The resulting FFT power maps in Figures 6 and S27 reveal a progression of well-defined phonon modes. We focus initially on the modes highlighted by PB, which should represent ground-state electron−phonon coupling. The modes observed in Pristine QD upon band-edge excitation (Figure 6(a)) closely match previous reports.[28] In Coupled QD we observe a systematic increase in the phonon frequency consistent with the lattice distortion induced by the introduction of inter-QD interactions (Figure 6(b)). In comparison to this PB band, we see in Figure 6 that in both films, the modes systematically shift to higher frequencies in the spectral regions corresponding to PIA and stimulated emission (SE). Moreover, the oscillations in these bands are out of phase with those in the PB band (Figure 6(c),(d)). Together, these observations reveal that the PIA and SE bands reflect excited-state electron−phonon couplings; that is, the excited species observed on band-edge excitation are fundamentally polaronic and the excitation of polarons induces

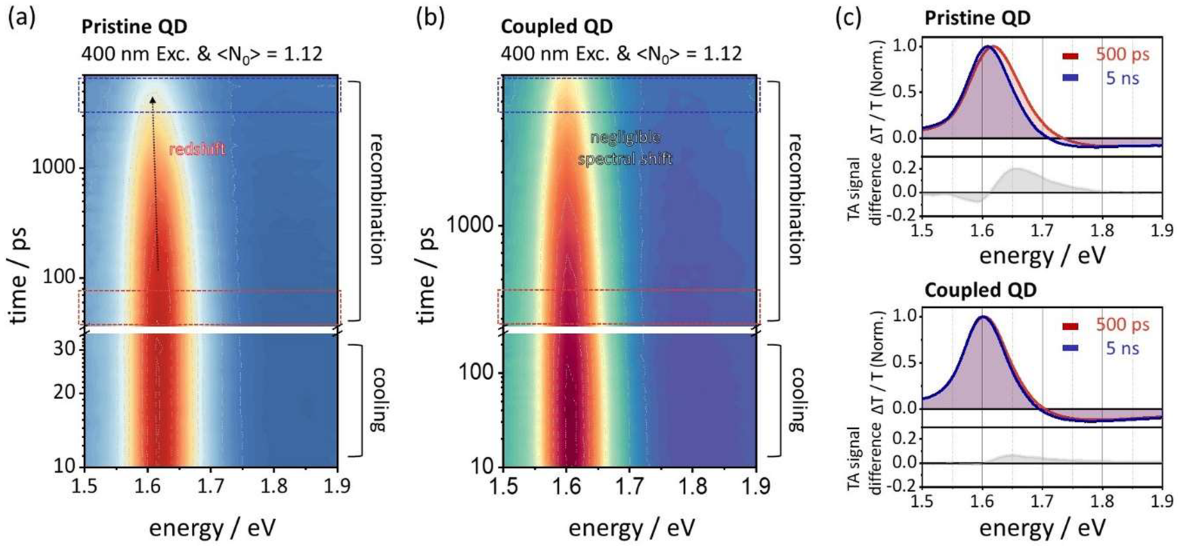

Figure 5. Coupling-dependent polaron recombination dynamics. fs-TA 2D contour maps up to 6 ns of (a) Pristine QD and (b) Coupled QD upon 400 nm excitation. (c) Two representative spectra at 500 ps and 5 ns and subtracted spectra (spectra at 500 ps − spectra at 5 ns) of Pristine QD (top) and Coupled QD (bottom).

Table 2. Kinetic Parameters for above Bandgap Excitation Results[a]

	Pristine QD/400 nm exc.				Coupled QD/400 nm exc.			
	$\tau_{\text{cooling 1}}$ (ps)/$\tau_{\text{cooling 2}}$ (ps)		$\tau_{\text{many-body}}$ (ps)	τ_{mono} (ns)	$\tau_{\text{cooling 1}}$ (ps)/$\tau_{\text{cooling 2}}$ (ps)		$\tau_{\text{many-body}}$ (ns)	τ_{mono} (ns)
$\langle N_0 \rangle = 0.14$	0.30	3.0		5.5	0.32	36		11
$\langle N_0 \rangle = 0.28$	0.32	3.1	550	5.5	0.30	38	4.3	11
$\langle N_0 \rangle = 0.56$	0.28	3.8	560	5.5	0.31	35	2.1	11
$\langle N_0 \rangle = 1.12$	0.29	3.6	520	5.5	0.29	33	1.2	11
$\langle N_0 \rangle = 2.24$	0.31	3.2	450	5.5	0.30	30	0.83	11

[a] Four time constants obtained from fs-TA decay profiles. Monomolecular lifetime is fixed by the time constant obtained by ns-PL measurements.

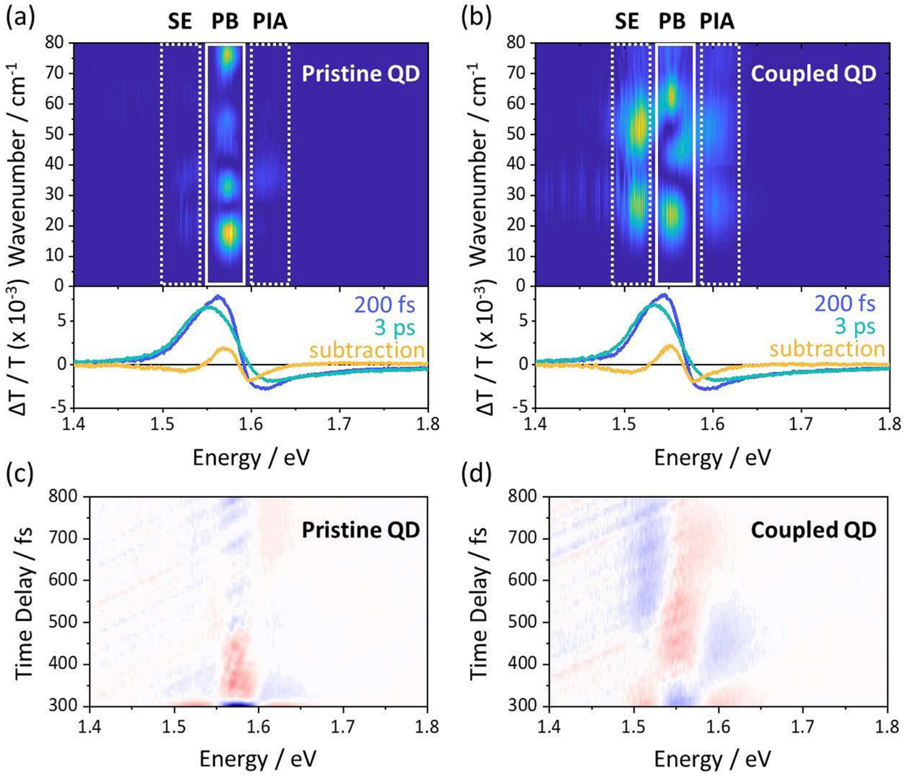

Figure 6. Electron−phonon couplings in QD films. 2D contour plot of FFT spectrum and representative TA spectra of (a) Pristine QD and (b) Coupled QD. Yellow "subtraction" spectra are obtained by subtracting the spectrum at 200 fs by the spectrum at 3 ps. 2D contour plot of TA residuals after exponential fitting of (c) Pristine QD and (d) Coupled QD revealing phase differences in the three detection bands.

some lattice deformation. Upon above-gap excitation, the phonon mode spectrum is redistributed toward lower frequencies with the appearance of a distinct node at the PB band position (Figure S28), consistent with prior observations.[24,26,30] Quantitative analysis of the detected modes is complicated by a strong ground-state contribution from modulation of the energy of the band-edge states.[24] Nevertheless, we note that the phonon frequencies in Pristine QD in this regime are similar to the excited-state (PIA and SE) phonons following band-edge excitation. Moreover, whereas the mode profiles in Pristine QD and Coupled QD are similar following band-edge excitation, we detect a markedly broader distribution of higher frequency modes in Coupled QD following the above-gap excitation. This effect is consistent with a different type of polaron forming in this sample.

Ultrafast Transient Absorption Spectroscopy. The fs-TA results at RT and 140 K show clearly that primary photoexcitations in QD films are polarons, and their polaron dynamics diverge when excess photon energy is exerted. Our observations indicate a difference in the nature of photoexcitations in the two films, but on the time scales accessible in our fs-TA experiment (instrument response 180 fs) the spectral differences associated with these states are very subtle (Figure 2). We thus extend our analysis into the thermalization time scale using excitation with compressed broadband pulses with sub-10 fs duration. The pulses spanned the range 520−680 nm and thus provided above-gap excitation (see the Method section for details).

The results for Pristine QD and Coupled QD are divided in Figure 7 into sub-100 and 100 fs to 1 ps ranges. On the longer time scale, both films reveal the typical spectral evolution associated with subpicosecond cooling processes reported above using fs-TA spectroscopy. Below 100 fs (Figure 7(a), (c)) we detect a new kinetic component (70−80 fs) which corresponds to the redistribution of PB band intensity during charge carrier thermalization.[57] In this regime, the spectral evolutions in the two QD films are strikingly different. Given their similar band structures in the range of the excitation pulse (Figure 1), this difference is surprising: similarly hot carriers are excited, and they should relax to equivalent distributions near the band edge. Interestingly, we found that the spectral difference can be precisely accounted for by the signature of

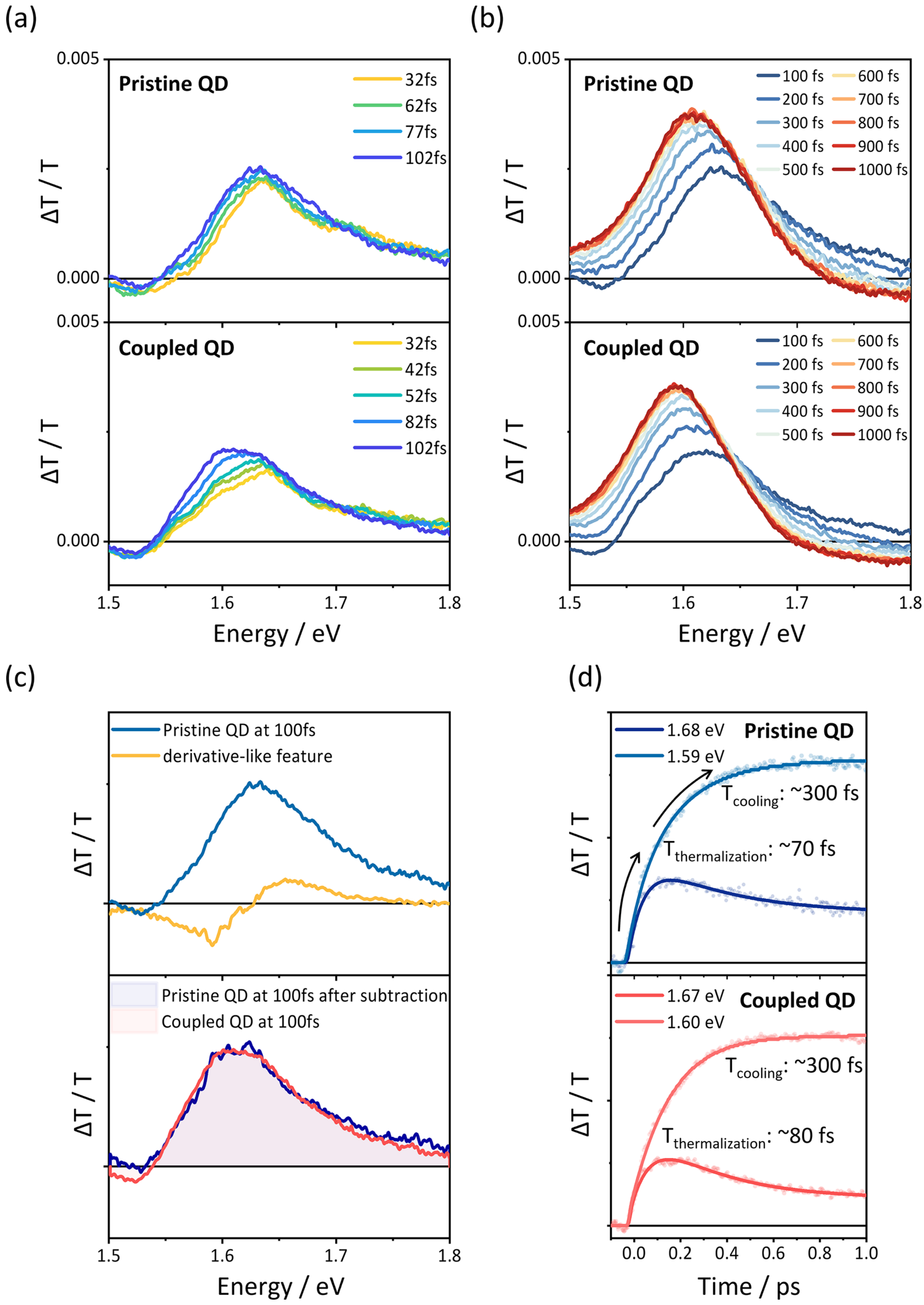

Figure 7. Ultrafast dynamics in QD films. Ultrafast TA spectra of Pristine QD and Coupled QD (a) up to 100 fs and (b) up to 1 ps. (c) Derivative-like spectral evolutions in fs-TA (λ_{exc} = 780) and TA spectrum at 100 fs of Pristine QD are visualized together in the top panel. The subtracted spectrum of Pristine QD (spectrum at 100 fs−derivative-like feature) is compared directly with the TA spectrum at 100 fs of Coupled QD in the bottom panel. (d) Ultrafast TA temporal profiles of Pristine QD and Coupled QD are plotted.

single-QD processes identified above. We recall the derivative-like line shape determined from spectral subtraction in Pristine QD under band-edge conditions in fs-TA (Figures 3 and 4). If we subtract this line shape from the Pristine QD spectrum at 100 fs, we obtain an excellent match to the equivalent spectrum of Coupled QD (Figure 7(c)). This result reveals that both films exhibit the same basic carrier thermalization behavior (broad envelope in Coupled QD < 100 fs), but in

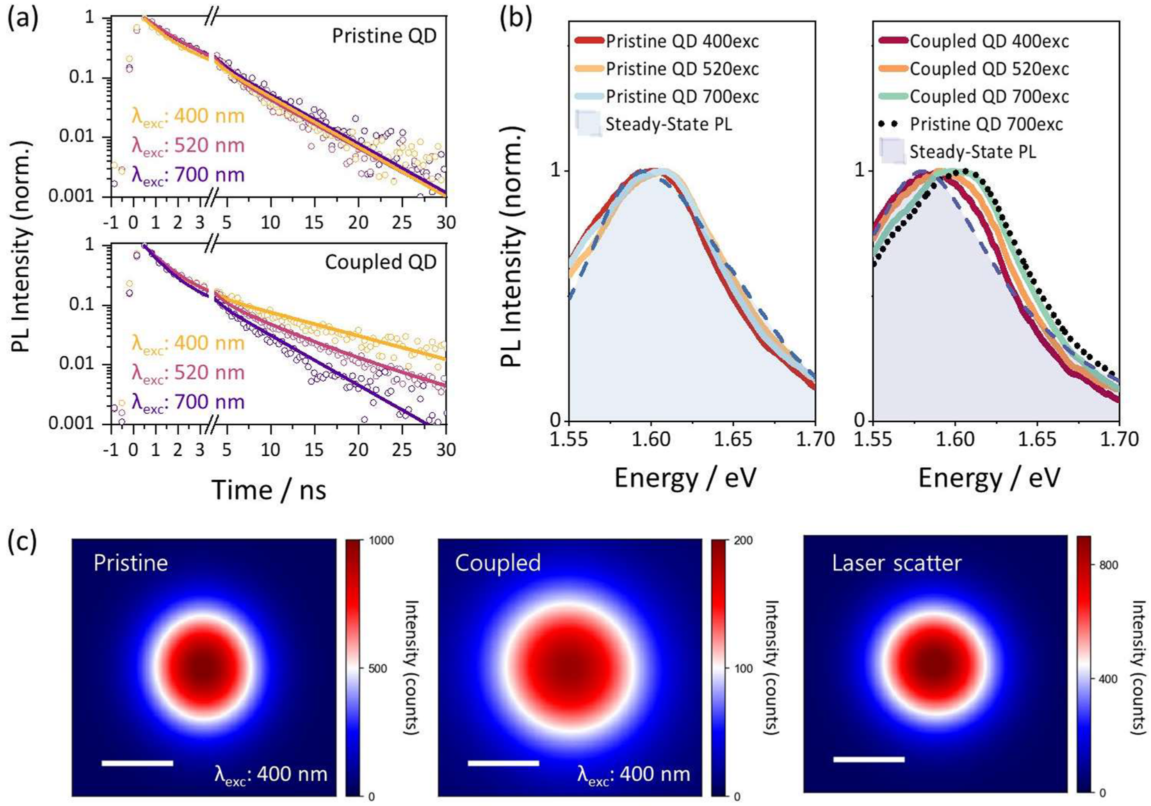

Figure 8. Long-time polaron recombination and transport via PL. (a) Time-resolved PL decay profiles of the two QD films depending on photoexcitation wavelength. (b) Time-resolved PL spectra (averaged from 0 to 10 ns, lines) and overlaid steady-state PL spectra (dashed and filled) of Pristine QD (left) and Coupled QD (right). (c) Spatial diffusion profile of Pristine QD, Coupled QD, and reference profile of laser scatter.

Pristine QD it competes with a distinct single-QD polaronic process. Thus, despite their apparent similarity, the excitation pathways in Pristine QD and Coupled QD diverge fundamentally on ultrafast time scales, and this branching defines all subsequent polaron behaviors. Indeed, our collected observations suggest that most of the excited species in Pristine QD evolve to the state signified by this derivative-like feature, which we assign below to polaronic excitons.

Time Resolved and Spatially Resolved PL. To capture how these different polaronic species behave on long time scales, we turn to complementary time-resolved PL measurements that more sensitively probe the monomolecular polaron lifetime. Regardless of excitation wavelength, Pristine QD shows nearly invariant PL decay profiles and consistent time-integrated PL spectra up to 10 ns (Figure 8). The dynamics are fitted by two exponents with lifetimes ~1 and ~5.5 ns, attributed to many-body processes and the monomolecular lifetime from comparison with our fs-TA kinetic analysis in Figure S12. As above, we only observe an important variation in Coupled QD excited above the bandgap. Nearly band-edge pumping at 700 nm (chosen to minimize pump scatter) shows a monomolecular lifetime of ~5 ns, but 400 nm excitation produces a long-lived polaron whose monomolecular lifetime is ~11 ns, in good agreement with the fs-TA results. The magnitude of the long-lived polaron population, as inferred from the relative weight of the long-lifetime component, significantly increases with increasing excitation energy. These effects are associated with slight spectral shifts (Figure 8(b)). Upon 700 nm excitation, the time-integrated PL spectra of Coupled QD match those of Pristine QD. As excitation energy increases, the PL spectra progressively redshift. This distribution of emitting states results in the asymmetric PL line shape reported in Figure 1(b) under white-light irradiation. To further explore whether the PL yield also changes in accompanying the spectral changes observed, we conduct steady-state PL measurements (Figure S29) with the excitation wavelength spanning from 700 to 400 nm. In contrast to the nearly constant intensities of the Pristine QD, the Coupled QD exhibits a significant drop as the excitation wavelength moves from 700 to 400 nm. These results again imply that the polaronic species generated by the above-bandgap excitation are qualitatively different between Coupled QD and Pristine QD.

In a final demonstration of these differences, we explore the spatial diffusion of the polaron populations using a PL mapping technique (Figure S30). We used excitation at 400 nm, where the most pronounced photophysical differences between Pristine QD and Coupled QD are observed. As shown in Figure 8(c), Pristine QD shows a confined spatial diffusion profile of polarons, with a σ_{average} of 6.28 μm, which is within the same order of magnitude as the profile of the excitation laser scatter (σ_{average} = 6.36 μm). In Coupled QD, the charge carriers have a much longer diffusion length, with a σ_{average} of 8.36 μm. This dramatic increase is due to the different nature of the polaronic species in the two films, which is itself governed by the different nanostructures revealed in Figure 1.

Polaron Dynamics Tuned by Inter-QD Interactions. We controlled the interactions between QDs by the removal of the native ligands on QD surfaces, which completely eliminates the edge-to-edge distance between QDs and brings QDs into

Scheme 1. Schematic of Polaron Dynamics in QD-Based Films

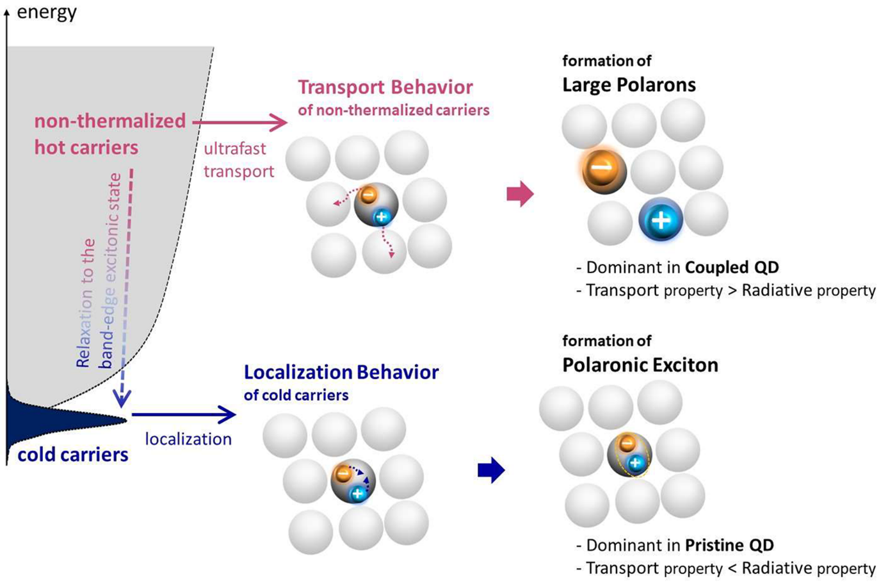

contact. While the QDs are in contact with each other, they are not likely to grow into bulk crystals due to the absence of excess energy for recrystallization. As shown in Figure 8(a), Pristine QD and Coupled QD show identical PL peak positions under band-edge excitation, suggesting that the quantum confinement of the QD building block is preserved after ligand removal. As shown in Figure 1(a), in Coupled QD, the size of the QDs remains unchanged, and the QDs are confined in at least one dimension. At the same time, after ligand removal, the facet-to-facet interactions between QDs drive them into a uniform orientation,[54] potentially establishing channels for carrier transport and enabling nuclear polarization to extend across the QD boundaries to form large polarons. As a result of these structural changes and the subtle interaction between the neighboring QDs they introduce, we observe fundamental photophysical distinctions between these two types of film. Pristine QD has strong dielectric barriers between QDs and is dominated by single-QD processes. The signature of the Coupled QD is a pronounced pump photon energy dependence, which can result in longer-lived polarons that diffuse much further than that in Pristine QD. We summarize the crucial polaron dynamics in these materials in Scheme 1. The similarity of the excited species in Pristine QD and Colloidal QD and our observation of standard polaronic signatures in Figures 2(a) and 3(a) indicate that Pristine QD hosts small polarons.[44] In contrast to bulk films (Figures S31−32) the carriers in Pristine QD and Colloidal QD have no pathway for long-range separation and instead remain confined in close proximity. The resulting states could be either self-trapped excitons or polaronic excitons.[67−70] However, the self-trapped exciton exhibits characteristic broad and featureless PL line shape due to its optically dark nature,[68−70] in contrast to the sharp PL we observe here (Figure 8). Instead, we highlight the rapid (<0.5 ps) fs-TA spectral changes to the polaron population we observe following band-edge excitation. These changes can be captured as the growth of a derivative-like feature centered at the band edge (Figure 3(b)). We consider this feature to be evidence of a Coulombically bound polaron pair (polaronic exciton) formation in a single QD.[67] Such weakly bound polaron pairs are well-known in organic semiconducting materials and characterized by their optically induced Stark effect.[71,72] In perovskite materials, reports of the Stark effect have centered around photon-dressed Floquet states and external electric-field-induced modulations.[73−77] The latter induces a spectral redshift of the band-edge excitonic state that produces similar lineshapes to what we have extracted from our fs-TA measurements in Figure 4(c).[76,77] Here, in contrast, the Stark effect originates from the separated charges that constitute the polaronic exciton. Though the state is neutral overall, the local charge imbalance results in a local electric field which perturbs the rest of the QD, causing a red-shift of the band-edge excitonic transition as shown in Figure 3(b) and Figure 4(c). The appearance of this Stark effect signature reveals that the charges generated upon band-edge excitation rapidly localize within the parent QD and form a polaronic exciton, likely driven by the Raman modes coupled to the excitonic transition.[78] This small polaron description is supported by the distinct increase in excited-state versus ground-state phonon frequencies detected in our low-temperature FFT analysis (Figure 6). Due to this localized character and the use of a similar QD unit across all samples, we capture nearly identical polaronic exciton behavior in Colloidal QD, Pristine QD, and Coupled QD when excited at the band edge.

We observe a significant change in the polaron behavior only in Coupled QD, and only following the generation of nonequilibrium hot carriers through above-bandgap excitation. We propose that the primary species generated in this regime are large polarons. The inter-QD interactions in this sample enable ultrafast transport of hot carriers, analogous to the ballistic transport of nonequilibrium carriers reported in lead halide perovskite bulk films,[79] though Coupled QD is distinctly intermediate between QD and bulk-like behavior. An important parameter to understand transport phenomena in QD-based materials is the degree of delocalization. Ligand treatments on CdSe QDs enhance their electronic delocalization, resulting in a 200% increase in exciton size.[80] Since the averaged size of FAPbI$_3$ QDs in our samples is on the same order as the exciton Bohr radius, we expect only a subtle elongation of the electronic wave function over neighboring

QDs. Thus, Coupled QD should exhibit reduced barriers for charge transport and hence enhanced charge diffusion length, as consistent with our PL mapping (Figure 8(c)).[81] This ultrafast transport of hot carriers is in direct competition with nonadiabatic relaxation to the band-edge states to form polaronic excitons. Upon sufficient spatial separation of electron and hole, their Coulombic interactions become negligible, facilitating long-range coupling with phonons to form large polarons with different cooling and recombination behavior.

This model would suggest that Coupled QD behaves as a hybrid between the strongly localized $FAPbI_3$ QD and bulk $FAPbI_3$. For comparison, we have prepared and performed equivalent fs-TA analysis on a bulk $FAPbI_3$ film (Figures S31−S33). We detect none of the spectral signatures of polaronic exciton formation, the hallmark of confined single-QD processes, because the charged species formed in the bulk are not spatially constrained (Figure S32). Indeed, the fs-TA dynamics are nearly identical for the above bandgap and band-edge excitation conditions, which suggests the excited-state processes are dominated by free charges or polarons regardless of pump photon energy. The principal difference from Coupled QD films is that the many-body processes are accelerated in the bulk film owing to enhanced diffusivity of carriers or polarons, though they share analogous pump fluence dependence. This similarity in behavior points to common fundamental properties: the charge carriers in the bulk film and large polarons in Coupled QD are diffusive, and their many-body processes originate from nongeminate encounters. Further discussion of the excited-state dynamics of the bulk film is presented in the supplementary note.

Depending on the nature of the polaronic species formed in the QD films, the cooling dynamics proceed through multiple stages. Following above-bandgap excitation, hot polarons in Colloidal QD, Pristine QD, and Coupled QD equilibrate with the lattice with time constants of ~300 fs (Figures 4(b) and 7(d)). Beyond this fast cooling process, we observe further relaxation on picosecond time scales (Figure 2(b),(d)), during which the PB band gains intensity and the high-energy shoulder band is reduced. Shifts on these time scales could potentially stem from relaxation through a disordered manifold of QDs from high-bandgap to low-bandgap sites, but this process should be accompanied by a shift of the PB peak which we do not observe. Instead, we find that these features are most consistent with a slower secondary cooling process that dissipates residual thermal energy (Figure S34). The secondary cooling processes are apparent in all of our $FAPbI_3$ QD-based materials from the lowest pump fluence ($<N_0 \geq 0.14$) for both 400 and 520 nm excitation and represent an intrinsic material property. Proposed mechanisms of hot carrier cooling processes include hot-phonon bottlenecks and large polaron effects.[82−85] In the latter case, nuclear polarization around the large polaron contributes to the reduction of scattering events with longitudinal optical phonon modes, which normally act as an important heat reservoir to dissipate the excess energy of hot polaron.[85] From our comparison across QD samples, we infer that the dominant contribution comes from such suppression of optical phonon relaxation due to quantum confinement in QDs, as reported for hot carrier cooling in $MAPbBr_3$ nanocrystals versus bulk film.[84] The effect is most prominent in the presence of large polarons in Coupled QD, where the secondary cooling channel is an order of magnitude slower than that in Pristine QD ($\tau_{\text{cooling 2}} \sim 40$ ps versus $\tau_{\text{cooling 2}} \sim 3$ ps).

The ultimate charge-carrier lifetime likewise depends strongly on the type of polaron present. In the case of band-edge excitation, the polaronic excitons observed in both film types exhibit comparable recombination time constants of $\tau_{\text{mono}} \sim 5.5$ ns (Figures S12−S15), which we take as the intrinsic lifetime. The faster decay channel ($\tau_{\text{many-body}}$) active at higher excitation densities can be attributed to bimolecular annihilation. Regardless of the decay channel, we observe no spectral evolution during the recombination of polaronic excitons in either film, indicating a pure population that relaxes to the ground state (Figure S11). That is no longer the case following above-bandgap excitation. In Pristine QD, excitation at 400 nm returns a similar polaron lifetime ($\tau_{\text{mono}} = 5.5$ ns) to the band-edge result. However, spectral evolution during recombination points to an interplay between multiple species. Using the spectral subtraction process in Figure 5(c), applied before and after recombination, we recover a Stark-effect line shape similar to that assigned to polaronic exciton formation in Figure 3. However, the sign in this case is reversed, pointing to the loss of polaronic exciton population. The residual polaron signal is a signature of a small population of long-lived polarons, which can form in a minority pathway through weak inter-QD coupling. Coupled QD is instead dominated by a large polaron population in excess-energy conditions (λ_{exc} = 400 and 520 nm), and we observe a distinctly longer intrinsic lifetime of $\tau_{\text{mono}} \sim 11$ ns (Figure S13). This behavior reflects that the large polaron is shielded by nuclear polarization via long-range Coulombic coupling with phonons, which deters radiative recombination and enhances its lifetime.[86] As shown in Figure 5, we can best capture the subtle spectral evolution during recombination through spectral subtraction, and the resulting difference spectrum is a manifestation of the Moss-Burstein effect (Figure 5(c)).[87] Following excitation at intermediate energy (520 nm), we capture a small contribution from the same reversed Stark-effect line shape seen in Pristine QD. Thus, the intermediate excitation results in detectable branching between large polarons and polaronic excitons formed via nonadiabatic relaxation to the band-edge states (Figure S7).

CONCLUSION

Through our combination of controlled inter-QD interactions and thorough time-resolved spectroscopic measurements, we demonstrated how to tune between small and large polaronic species within one of the widespread hybrid perovskite compositions. Both large polarons and small polaronic excitons are intrinsic to these low bandgap perovskite materials, and their balance is gated by a combination of inter-QD coupling and excess pump energy to access more delocalized electronic states. Once the polaronic species are formed following the initial thermalization, they exhibit important differences in their cooling and recombination pathways. The competition we observe between the formation of large polarons and polaronic excitons suggests that the detailed polaron dynamics should be revisited in other bulk materials composed of nanostructured components, as these may provide the subtle confinement needed to bias one channel over the other. Richer understanding of how to controllably form these species will enhance the practical applications of perovskite materials: the polaronic exciton provides a higher PL quantum yield despite its shorter lifetime, whereas large polarons afford much more rapid transport, slow carrier cooling, and an lengthen lifetime.

METHODS

Chemicals. Oleylamine (OAm, 70%), oleic acid (OA, 90%), 1-octadecene (ODE, 90%), octane (anhydrous, 99%), hexane (95%), methyl acetate (MeOAc, anhydrous, 99.5%), and formamidinium acetate (FAOAc, 99%) were purchased from Sigma-Aldrich (St. Louis, Missouri). Lead(II) iodide (PbI_2, 99.99%) was purchased from TCI Chemicals. All of the chemicals were used as purchased without purification.

$FAPbI_3$ QD Synthesis. $FAPbI_3$ QDs were synthesized following our reported methods with some modifications.[54] In a 50 mL three-neck round-bottom flask, 521 mg of FAOAc and 10 mL of OA were mixed and degassed under vacuum at 110 °C for 30 min. After a clear solution was obtained, N_2 was placed in the flask. The FA-oleate solution was cooled to 80 °C and ready for injection. In another 100 mL three-neck round-bottom flask, 400 mg of PbI_2, 20 mL of ODE, 3 mL of OA, and 3 mL of OAm were mixed and degassed under vacuum at 120 °C for 30 min. After a clear solution was obtained, N_2 was flowed into the flask and the PbI_2 solution was cooled to 80 °C. Then 5 mL of FA-oleate solution was swiftly injected into the PbI_2 solution. After about 15 s, the reaction was quenched with an ice bath. The crude product was mixed with 6 mL of MeOAc and centrifuged at 8000 rpm for 10 min. The precipitated QDs were dispersed in 10 mL of hexane. The QDs were precipitated again with MeOAc (MeOAc:hexane = 1:1) at 8000 rpm for 10 min. The resulting precipitate was redispersed in octane at a concentration of 65 mg/mL for spin coating.

$FAPbI_3$ QD Film Preparation. The pristine QD films were deposited by spin coating the QD solution (60 mg/mL in octane) at 2000 rpm for 25 s. This results in ~70 nm thick films (roughly 5 monolayers of QDs). The coupled QD films were prepared by swiftly dipping the pristine QD films into MeOAc for 5 s, rinsing with neat MeOAc for 1 s, and blowing them dry with a stream of N_2. All the depositions were performed in ambient conditions with 30−40% relative humidity.

Characterizations of QD Solutions and Films. Transmission electron microscopic (TEM) images were acquired using an FEI Tecnai 12 BioTwin TEM. Ultraviolet−visible (UV−vis) absorption spectra were collected using an Agilent Cary 5000 UV−vis−NIR spectrometer with diffuse reflectance accessories (DRA). The steady-state photoluminescence spectra of QD films were recorded with a home-built photoluminescence spectrometer based on an Avantes miniature spectrometer (Avaspec-Mini-4096CL).

Time-Resolved Optical Spectroscopy. Transient absorption measurements were conducted with an automated transient absorption spectrometer (HELIOS, Ultrafast Systems) driven by the Yb:KGW amplifier (PHAROS-SP, Light Conversion) operating at 8 kHz. An optical parametric amplifier (OPA) and its second harmonic (SH) module (ORPHEUS and LYRA-SH, Light Conversion), pumped by the same Yb:KGW amplifier, generated a 200 fs narrowband pump pulse. A portion of the fundamental was separated to generate a white light continuum probe pulse ranging from 2.53 to 1.35 eV by using a 1 cm YAG crystal. The beam diameters ($1/e^2$ height) for pump and probe pulses at the sample position were 650 and 75 μm, respectively. TA spectra were collected with the magic angle condition between pump and probe and in a shot-to-shot fashion. Pump−probe time delay was set by a mechanical delay stage from −3 to 7000 ps. For low temperature experiments (140 K), the samples were cooled in a liquid nitrogen cryostat (Janis VPF-100, Janis Research Company, LLC) under vacuum conditions. Time-resolved PL measurements were performed using an ICCD detector (PI-MAX4, Princeton Instruments) and the same OPA and SH modules used in the transient absorption experiments (ORPHEUS and LYRA-SH, Light Conversion) to generate tunable narrowband excitation pulses (200 fs). For time-integrated PL spectra, the repetitive mode with a 10 ns gate window was used, whereas for time-resolved PL, the sequential mode with a 0.48 ns gate window was utilized.

Ultrafast Transient Absorption Spectroscopy and Pulse Characterization. All ultrafast transient absorption (TA) measurements were performed using a home-built setup driven by the Yb:KGW amplifier (PHAROS-SP, Light Conversion) operating at 8 kHz; 6 W of the output was directed into a commercially available HIRO (Light Conversion) for frequency doubling (515 nm, 0.5 W) and subsequent sum frequency generation (343 nm, 0.375 W). The 343 nm output was used as pump sources for noncollinear optical parametric amplifiers (NOPA) that spanned the visible (520 nm−680 nm, VIS NOPA) wavelength ranges (Figure S36). 40−50 μW of the fundamental was focused into 3 mm sapphire windows for white light continuum (WLC) generation to be used as a seed. The pump and seed were temporally and spatially overlapped in a 2 mm BBO crystal (Eksma, $\theta = 31.5°$, Type I). After amplification, pulses were directed through a chopper (Thorlabs, MC2000B) and compressed using a chirped mirror (Laser Quantum, DCM9, 20 bounces) and wedge pairs (Newport, 23RQ12-02-M). They were then directed into either the ultrafast TA setup or a second harmonic generation frequency resolved optical gating (SHG-FROG) setup to measure the pulse duration. The pulse duration was extracted by using FROG software by Femtosoft Technologies, and the raw SHG-FOG traces and intensity profiles are shown in Figure S36. Pulse durations were also verified to resolve solvent oscillations in acetonitrile solvent in a transient absorption measurement. To generate the probe used in ultrafast TA measurements, a separate WLC was generated in identical fashion to that implemented in the NOPA. This probe was delayed relative to the NOPA using a piezo stage (Thorlabs, PDX1), and the pulses were focused onto the sample by the same spherical mirror. The probe was collected after transmission through the sample and dispersed onto a CMOS detector (Stresing, 3010, HA:S12198-1024). The pump and probe spot sizes were set to 300 and 80 μm, respectively. A step size of 5 fs was used during TA scans, and 4000 pump on/off spectra were collected per time point in a shot-to-shot fashion using custom LabVIEW software.

Photoluminescence Mapping. Spatial diffusion profiles were measured on an inverted microscope (Olympus IX 81). Samples were excited with the 400 nm 8 MHz repetition laser (Mai Tai Spectra-Physics). The excitation beam is focused through a 100×, 1.4 NA oil immersion objective (Olympus UPLSAPO), and photoluminescence was collected through a 60×, 0.7 NA air objective (Olympus LUCPlanFLN) which is placed on a piezo-nanopositioning stage (PI P-733.3CD). The collected light is transferred through a combination of 488 nm long pass filter and a 770 nm/50 nm bandpass filter and then imaged onto a single-photon-counting avalanche photodiode (single photon counting modules (SPCM) COUNT Photon Counter from Laser Components). Data acquisition was performed with SymPhoTime 64 software (PicoQuant, Germany).

ASSOCIATED CONTENT

Supporting Information

The Supporting Information is available free of charge at https://pubs.acs.org/doi/10.1021/acsnano.3c08748.

> Distribution of QD edge length and edge-to-edge distances; Stokes shift in QD films; PL spectra of QD films; note for the calculation of $<N_0>$; fs-TA 2D contour map, hot polaron cooling kinetics and spectrum derivatives of QD films upon 520 nm excitation; fs-TA 2D contour map and spectrum derivatives of colloidal QD upon 400 and 780 nm excitations; fs-TA temporal profiles of Colloidal QD in solution depending on pump wavelength and fluence; fs-TA measurements of FAI surface-passivated Coupled QD; spectral evolution of QD films upon 780 nm excitation; fs-TA temporal profiles and subtracted spectra of QD films and colloidal QD; fs-TA 2D contour map and polaron cooling

dynamics of QD films at 140 K; derivative-like TA spectral evolutions upon band-edge excitations at 140 K; pump fluence dependent kinetics of QD films at 140 K; oscillatory features in fs-TA temporal profiles and 2D contour map of FFT spectra at 140 K; steady-state PL intensities of QD films under different excitation wavelengths; 3D surface plots of the spatial diffusion profiles of QD films; fs-TA 2D contour map, carrier dynamics and spectrum derivatives of $FAPbI_3$ bulk films; extracted carrier temperature calculation of QD films at different fluences; note for the calculation of extracted carrier temperature; excitation density dependence in the PIA band resulting from BGR; ultrafast TA measurements using the sub-10 fs noncollinear optical parametric amplifier (NOPA).; comparison of steady-state absorption and emission spectra of Pristine QD, Coupled QD, and bulk FAPbI3 film (PDF)

AUTHOR INFORMATION

Corresponding Authors

Andrew J. Musser − *Department of Chemistry and Chemical Biology, Cornell University, Ithaca, New York 14853, United States*; orcid.org/0000-0002-4600-6606; Email: ajm557@cornell.edu

Qiuming Yu − *Robert Frederick Smith School of Chemical and Biomolecular Engineering, Cornell University, Ithaca, New York 14853, United States*; orcid.org/0000-0002-2401-4664; Email: qy10@cornell.edu

Authors

Juno Kim − *Department of Chemistry and Chemical Biology, Cornell University, Ithaca, New York 14853, United States*

Yuanze Xu − *Robert Frederick Smith School of Chemical and Biomolecular Engineering, Cornell University, Ithaca, New York 14853, United States*; orcid.org/0000-0002-4873-6629

David Bain − *Department of Chemistry and Chemical Biology, Cornell University, Ithaca, New York 14853, United States*

Mingxing Li − *Center for Functional Nanomaterials, Brookhaven National Laboratory, Upton, New York 11973, United States*

Mircea Cotlet − *Center for Functional Nanomaterials, Brookhaven National Laboratory, Upton, New York 11973, United States*; orcid.org/0000-0002-5024-3540

Complete contact information is available at:
https://pubs.acs.org/10.1021/acsnano.3c08748

Author Contributions

[#]J.K. and Y.X. contributed equally. A.J.M. and Q.Y. conceived the project. Y.X. synthesized the samples and performed TEM measurements. J.K. and Y.X. conducted basic optical characterizations. J.K. performed the fs-TA and time-resolved PL experiments. J.K. and D.B. conducted ultrafast TA experiments. Y.X., M.L., and M.C. conducted PL mapping experiments. J.K., Y.X., Q.Y., and A.J.M. analyzed the data and wrote the paper with input from all authors.

Notes

The authors declare no competing financial interest.

ACKNOWLEDGMENTS

A.J.M. and J.K. were supported by the U.S. Department of Energy, Office of Science, Basic Energy Sciences, CPIMS Program under Early Career Research Program (Award No. DE-SC0021941). J.K. was supported by Basic Science Research Program through the National Research Foundation of Korea (NRF) funded by the Ministry of Education (2022R1A6A3A03072477). D.B. was supported by a Cornell University College of Arts and Sciences New Frontiers Grant. Q.Y. and Y.X. were financially supported by NSF ECCS-2054942 and EPM-2114350. This work made use of the Cornell Center for Materials Research shared facilities which are supported through the NSF MRSEC program (DMR-1719875). The PL mapping experiments used the resources from the Centre for Functional Nanomaterials at Brookhaven National Laboratory, supported by U.S. DOE Office of Science Facilities under Contract No. DE-SC0012704.

REFERENCES

(1) Kim, J. Y.; Lee, J.-Y.; Jung, H. S.; Shin, H.; Park, N.-G. High-efficiency perovskite solar cells. *Chem. Rev.* **2020**, *120*, 7867−7918.

(2) Yang, X.; Ma, L.; Li, L.; Luo, M.; Wang, X.; Gong, Q.; Lu, C.; Zhu, R. Towards micro-PeLED displays. *Nature Reviews Materials* **2023**, *8*, 341.

(3) Chen, Q.; Wu, J.; Ou, X.; Huang, B.; Almutlaq, J.; Zhumekenov, A. A.; Guan, X.; Han, S.; Liang, L.; Yi, Z.; Li, J.; Xie, X.; Wang, Y.; Li, Y.; Fan, D.; Teh, D. B. L.; All, A. H.; Mohammed, O. F.; Bakr, O. M.; Wu, T.; et al. All-inorganic perovskite nanocrystal scintillators. *Nature* **2018**, *561*, 88−93.

(4) Zhang, Q.; Shang, Q.; Su, R.; Do, T. H.; Xiong, Q. Halide perovskite semi-conductor lasers: materials, cavity design, and low threshold. *Nano Lett.* **2021**, *21*, 1903−1914.

(5) Manser, J. S.; Christians, J. A.; Kamat, P. V. Intriguing optoelectronic properties of metal halide perovskites. *Chem. Rev.* **2016**, *116*, 12956−13008.

(6) Buizza, L. R. V.; Herz, L. M. Polarons and Charge Localization in Metal-Halide Semiconductors for Photovoltaic and Light-Emitting Devices. *Adv. Mater.* **2021**, 33, 2007057.

(7) Ghosh, D.; Welch, E.; Neukirch, A. J.; Zakhidov, A.; Tretiak, S. Polarons in Halide Perovskites: A Perspective. *J. Phys. Chem. Lett.* **2020**, *11*, 3271−3286.

(8) Miyata, K.; Meggiolaro, D.; Trinh, M. T.; Joshi, P. P.; Mosconi, E.; Jones, S. C.; De Angelis, F.; Zhu, X.-Y. Large polarons in lead halide perovskites. *Sci. Adv.* **2017**, 3, e1701217.

(9) Miyata, K.; Zhu, X.-Y. Ferroelectric Large Polarons. *Nat. Mater.* **2018**, *17*, 379−384.

(10) Devreese, J. T.; Alexandrov, A. S. Frohlich polaron and bipolaron: recent developments. *Rep. Prog. Phys.* **2009**, 72, 066501.

(11) Yamada, Y.; Kanemitsu, Y. Electron-phonon interactions in halide perovskites. *NPG. Asia Mater.* **2022**, *14*, 48.

(12) Wright, A. D.; Verdi, C.; Milot, R. L.; Eperon, G. E.; Perez-Osorio, M. A.; Snaith, H. J.; Giustino, F.; Johnston, M. B.; Herz, L. M. Electron-phonon coupling in hybrid lead halide perovskites. *Nat. Commun.* **2016**, *7*, 11755.

(13) Fu, M.; Tamarat, P.; Trebbia, J.-B.; Bodnarchuk, M. I.; Kovalenko, M. V.; Even, J.; Lounis, B. Unraveling exciton−phonon coupling in individual $FAPbI_3$ nanocrystals emitting near-infrared single photons. *Nat. Commun.* **2018**, *9*, 3318.

(14) Bretschneider, S. A.; Ivanov, I.; Wang, H. I.; Miyata, K.; Zhu, X.; Bonn, M. Quantifying Polaron Formation and Charge Carrier Cooling in Lead-Iodide Perovskites. *Adv. Mater.* **2018**, *30*, 1707312.

(15) Cinquanta, E.; Meggiolaro, D.; Motti, S. G.; Gandini, M.; Alcocer, M. J. P.; Akkerman, Q. A.; Vozzi, C.; Manna, L.; De Angelis, F.; Petrozza, A.; Stagira, S. Ultrafast THz Probe of Photoinduced Polarons in Lead-Halide Perovskites. *Phys. Rev. Lett.* **2019**, *122*, 166601.

(16) Lan, Y.; Dringoli, B. J.; Valverde-Chavez, D. A.; Ponseca, C. S., Jr.; Sutton, M.; He, Y.; Kanatzidis, M. G.; Cooke, D. G. Ultrafast correlated charge and lattice motion in a hybrid metal halide perovskite. *Sci. Adv.* **2019**, *5*, aaw5558.

(17) Seiler, H.; Zahn, D.; Taylor, V. C. A.; Bodnarchuk, M. I.; Windsor, Y. W.; Kovalenko, M. V.; Ernstorfer, R. Direct Observation of Ultrafast Lattice Distortions during Exciton−Polaron Formation in Lead Halide Perovskite Nanocrystals. *ACS Nano* **2023**, *17*, 1979−1988.

(18) Guzelturk, B.; Winkler, T.; Van de Goor, T. W. J.; Smith, M. D.; Bourelle, S. A.; Feldmann, S.; Trigo, M.; Teitelbaum, S. W.; Steinruck, H.-G.; de la Pena, G. A.; Alonso-Mori, R.; Zhu, D.; Sato, T.; Karunadasa, H. I.; Toney, M. F.; Deschler, F.; Lindenberg, A. M. Visualization of dynamic polaronic strain fields in hybrid lead halide perovskites. *Nat. Mater.* **2021**, *20*, 618−623.

(19) Cannelli, O.; Colonna, N.; Puppin, M.; Rossi, T. C.; Kinschel, D.; Leroy, L. M. D.; Loffler, J.; Budarz, J. M.; March, A. M.; Doumy, G.; Haddad, A. A.; Tu, M.-F.; Kumagai, Y.; Walko, D.; Smolentsev, G.; Krieg, F.; Boehme, S. C.; Kovalenko, M. V.; Chergui, M.; Mancini, G. F. Quantifying Photoinduced Polaronic Distortions in Inorganic Lead Halide Perovskite Nanocrystals. *J. Am. Chem. Soc.* **2021**, *143*, 9048−9059.

(20) Kim, H.; Hunger, J.; Canovas, E.; Karakus, M.; Mics, Z.; Grechko, M.; Turchinovich, D.; Parekh, S. H.; Bonn, M. Direct observation of mode-specific phonon-band gap coupling in methylammonium lead halide perovskites. *Nat. Commun.* **2017**, *8*, 687.

(21) Wu, X.; Tan, L. Z.; Shen, X.; Hu, T.; Miyata, K.; Trinh, M. T.; Li, R.; Coffee, R.; Liu, S.; Egger, D. A.; Makasyuk, I.; Zheng, Q.; Fry, A.; Robinson, J. S.; Smith, M. D.; Guzelturk, B.; Karunadasa, H. I.; Wang, X.; Zhu, X.; Kronik, L.; Rappe, A. M.; Lindenberg, A. M. Light-induced picosecond rotational disordering of the inorganic sublattice in hybrid perovskites. *Sci. Adv.* **2017**, *3*, e1602388.

(22) Shrivastava, M.; Bodnarchuk, M. I.; Hazarika, A.; Luther, J. M.; Beard, M. C.; Kovalenko, M. V.; Adarsh, K. V. Polaron and Spin Dynamics in Organic−Inorganic Lead Halide Perovskite Nanocrystals. *Adv. Optical Mater.* **2020**, *8*, 2001016.

(23) Yue, X.; Wang, C.; Zhang, B.; Zhang, Z.; Xiong, Z.; Zu, X.; Liu, Z.; Hu, Z.; Odunmbaku, G. O.; Zheng, Y.; Sun, K.; Du, J. Real-time observation of the buildup of polaron in α-FAPbI$_3$. *Nat. Commun.* **2023**, *14*, 917.

(24) Fu, J.; Li, M.; Solanki, A.; Xu, Q.; Lekina, Y.; Ramesh, S.; Shen, Z. X.; Sum, T. C. Electronic States Modulation by Coherent Optical Phonons in 2D Halide Perovskites. *Adv. Mater.* **2021**, *33*, 2006233.

(25) Seiler, H.; Palato, S.; Sonnichsen, C.; Baker, H.; Socie, E.; Strandell, D. P.; Kambhampati, P. Two-dimensional electronic spectroscopy reveals liquid-like lineshape dynamics in CsPbI$_3$ perovskite nanocrystals. *Nat. Commun.* **2019**, *10*, 4962.

(26) Ghosh, T.; Aharon, S.; Etgar, L.; Ruhman, S. Free Carrier Emergence and Onset of Electron−Phonon Coupling in Methylammonium Lead Halide Perovskite Films. *J. Am. Chem. Soc.* **2017**, *139*, 18262−18270.

(27) Liu, Z.; Vaswani, C.; Yang, X.; Zhao, Y.; Yao, Y.; Song, Z.; Cheng, D.; Shi, Y.; Luo, L.; Mudiyanselage, D.-H.; Huang, C.; Park, J.-M.; Kim, R. H. J.; Zhao, J.; Yan, Y.; Ho, K.-M.; Wang, J. Ultrafast Control of Excitonic Rashba Fine Structure by Phonon Coherence in the Metal Halide Perovskite CH$_3$NH$_3$PbI$_3$. *Phys. Rev. Lett.* **2020**, *124*, 157401.

(28) Debnath, T.; Sarker, D.; Huang, H.; Han, Z.-K.; Dey, A.; Polavarapu, L.; Levchenko, S. V.; Feldmann, J. Coherent vibrational dynamics reveals lattice anharmonicity in organic−inorganic halide perovskite nanocrystals. *Nat. Commun.* **2021**, *12*, 2629.

(29) Ni, L.; Huynh, U.; Cheminal, A.; Thomas, T. H.; Shivanna, R.; Hinrichsen, T. F.; Ahmad, S.; Sadhanala, A.; Rao, A. Real-Time Observation of Exciton−Phonon Coupling Dynamics in Self-Assembled Hybrid Perovskite Quantum Wells. *ACS Nano* **2017**, *11*, 10834−10843.

(30) Duan, H.-G.; Tiwari, V.; Jha, A.; Berdiyorov, G. R.; Akimov, A.; Vendrell, O.; Nayak, P. K.; Snaith, H. J.; Thorwart, M.; Li, Z.; Madjet, M. E.; Miller, R. J. D. Photoinduced Vibrations Drive Ultrafast Structural Distortion in Lead Halide Perovskite. *J. Am. Chem. Soc.* **2020**, *142*, 16569−16578.

(31) Batignani, G.; Fumero, G.; Kandada, A. R. S.; Cerullo, G.; Gandini, M.; Ferrante, C.; Petrozza, A.; Scopigno, T. Probing femtosecond lattice displacement upon photo-carrier generation in lead halide perovskite. *Nat. Commun.* **2018**, *9*, 1971.

(32) Park, M.; Neukirch, A. J.; Reyes-Lillo, S. E.; Lai, M.; Ellis, S. R.; Dietze, D.; Neaton, J. B.; Yang, P.; Tretiak, S.; Mathies, R. A. Excited-state vibrational dynamics toward the polaron in methylammonium lead iodide perovskite. *Nat. Commun.* **2018**, *9*, 2525.

(33) Fu, J.; Ramesh, S.; Melvin Lim, J. W.; Sum, T. C. Carriers, Quasi-particles, and Collective Excitations in Halide Perovskites. *Chem. Rev.* **2023**, *123*, 8154−8231.

(34) Thouin, F.; Valverde-Chavez, D. A.; Quarti, C.; Cortecchia, D.; Bargigia, I.; Beljonne, D.; Petrozza, A.; Silva, C.; Srimath Kandada, A. R. Phonon coherences reveal the polaronic character of excitons in two-dimensional lead halide perovskites. *Nat. Mater.* **2019**, *18*, 349−356.

(35) Srimath Kandada, A. R.; Silva, C. Exciton Polarons in Two-Dimensional Hybrid Metal-Halide Perovskites. *J. Phys. Chem. Lett.* **2020**, *11*, 3173−3184.

(36) Yin, J.; Li, H.; Cortecchia, D.; Soci, C.; Bredas, J.-L. Excitonic and Polaronic Properties of 2D Hybrid Organic−Inorganic Perovskites. *ACS Energy. Lett.* **2017**, *2*, 417−423.

(37) Wong, W. P. D.; Yin, J.; Chaudhary, B.; Chin, X. Y.; Cortecchia, D.; Lo, S. -Z. A.; Grimsdale, A. C.; Mohammed, O. F.; Lanzani, G.; Soci, C. Large Polaron Self-Trapped States in Three-Dimensional Metal-Halide Perovskites. *ACS Energy. Lett.* **2020**, *2*, 20−27.

(38) Zhang, Z.; Long, R.; Tokina, M. V.; Prezhdo, O. V. Interplay between Localized and Free Charge Carriers Can Explain Hot Fluorescence in the CH$_3$NH$_3$PbBr$_3$ Perovskite: Time-Domain Ab Initio Analysis. *J. Am. Chem. Soc.* **2017**, *139*, 17327−17333.

(39) Poonia, A. K.; Shrivastava, M.; Mir, W. J.; Aneesh, J.; Nag, A.; Adarsh, A. V. Intervalley polaronic biexcitons in metal halide perovskite quantum dots. *Phys. Rev. B* **2021**, *104*, L161407.

(40) Srimath Kandada, A. R.; Petrozza, A. Photophysics of Hybrid Lead Halide Perovskites: The Role of Microstructure. *Acc. Chem. Res.* **2016**, *49*, 536−544.

(41) Liu, L.; Najar, A.; Wang, K.; Du, M.; Liu, S. Perovskite Quantum Dots in Solar Cells. *Adv. Sci.* **2022**, *9*, 2104577.

(42) Kagan, C. R.; Straus, D. B. Photophysics of Two-Dimensional Semiconducting Organic-Inorganic Metal-Halide Perovskites. *Annu. Rev. Phys. Chem.* **2022**, *73*, 403−428.

(43) deQuilettes, D. W.; Vorpahl, S. M.; Stranks, S. D.; Nagaoka, H.; Eperon, G. E.; Ziffer, M. E.; Snaith, H. J.; Ginger, D. S. Impact of microstructure on local carrier lifetime in perovskite solar cells. *Science* **2015**, *348*, 683−686.

(44) Franchini, C.; Reticcioli, M.; Setvin, M.; Diebold, U. Polarons in materials. *Nat. Rev. Mater.* **2021**, *6*, 560−586.

(45) Bai, Y.; Hao, M.; Ding, S.; Chen, P.; Wang, L. Surface chemistry engineering of perovskite quantum dots: strategies, applications, and perspectives. *Adv. Mater.* **2022**, *34*, 2105958.

(46) Kagan, C. R.; Lifshitz, E.; Sargent, E. H.; Talapin, D. V. Building devices from colloidal quantum dots. *Science* **2016**, *353*, 6302.

(47) Zhang, Z.; Sung, J.; Toolan, D. T. W.; Han, S.; Pandya, R.; Weir, M. P.; Xiao, J.; Dowland, S.; Liu, M.; Ryan, A. J.; Jones, R. A. L.; Huang, S.; Rao, A. Ultrafast exciton transport at early times in quantum dot solids. *Nat. Mater.* **2022**, *21*, 533−539.

(48) Vickers, E. T.; Enlow, E. E.; Delmas, W. G.; DiBenedetto, A. C.; Chowdhury, A. H.; Bahrami, B.; Dreskin, B. W.; Graham, T. A.; Hernandez, I. N.; Carter, S. A.; Ghosh, S.; Qiao, Q.; Zhang, J. Z. Enhancing Charge Carrier Delocalization in Perovskite Quantum Dot Solids with Energetically Aligned Conjugated Capping Ligands. *ACS Energy Lett.* **2020**, *5*, 817−825.

(49) Zhumekenov, A. A.; Saidaminov, M. I.; Haque, M. A.; Alarousu, E.; Sarmah, S. P.; Murali, B.; Dursun, I.; Miao, X.-H.; Abdelhady, A. L.; Wu, T.; Mohammed, O. F.; Bakr, O. M. Formamidinium Lead Halide Perovskite Crystals with Unprecedented Long Carrier Dynamics and Diffusion Length. *ACS Energy Lett.* **2016**, *1*, 32−37.

(50) Rehman, W.; Milot, R. L.; Eperon, G. E.; Wehrenfennig, C.; Boland, J. L.; Snaith, H. J.; Johnston, M. B.; Herz, L. M. Charge-

Carrier Dynamics and Mobilities in Formamidinium Lead Mixed-Halide Perovskites. *Adv. Mater.* **2015**, *27*, 7938−7944.

(51) Galkowski, K.; Mitioglu, A.; Miyata, A.; Plochocka, P.; Portugall, O.; Eperon, G. E.; Wang, J. T.; Stergiopoulos, T.; Stranks, S. D.; Snaith, H. J.; Nicholas, R. J. Determination of the exciton binding energy and effective masses for methylammonium and formamidinium lead tri-halide perovskite semiconductors. *Energy Environ. Sci.* **2016**, *9*, 962.

(52) Elmestekawy, K. A.; Wright, A. D.; Lohmann, K. B.; Borchert, J.; Johnston, M. B.; Herz, L. M. Controlling Intrinsic Quantum Confinement in Formamidinium Lead Triiodide Perov-skite through Cs Substitution. *ACS Nano* **2022**, *16*, 9640−9650.

(53) Wright, A. D.; Volonakis, G.; Borchert, J.; Davies, C. L.; Giustino, F.; Johnston, M. B.; Herz, L. M. Intrinsic quantum confinement in formamidinium lead triiodide perovskite. *Nat. Mater.* **2020**, *19*, 1201−1206.

(54) Xu, Y.; Li, H.; Ramakrishnan, S.; Song, D.; Zhang, Y.; Cotlet, M.; Yu, Q. Ion-Assisted Ligand Exchange for Efficient and Stable Inverted $FAPbI_3$ Quantum Dot Solar Cells. *ACS Appl. Energy Mater.* **2022**, *5*, 9858−9869.

(55) Papagiorgis, P.; Protesescu, L.; Kovalenko, M. V.; Othonos, A.; Itskos, G. Long-Lived Hot Carriers in Formamidinium Lead Iodide Nanocrystals. *J. Phys. Chem. C* **2017**, *121*, 12434−12440.

(56) Yang, Y.; Ostrowski, D. P.; France, R. M.; Zhu, K.; van de Lagemaat, J.; Luther, J. M.; Beard, M. C. Observation of a hot-phonon bottleneck in lead-iodide perovskites. *Nat. Photonics* **2016**, *10*, 53−59.

(57) Richter, J. M.; Branchi, F.; Valduga de Almeida Camargo, F.; Zhao, B.; Friend, R. H.; Cerullo, G.; Deschler, F. Ultrafast carrier thermalization in lead iodide perovskite probed with two-dimensional electronic Spectroscopy. *Nat. Commun.* **2017**, *8*, 376.

(58) Price, M. B.; Butkus, J.; Jellicoe, T. C.; Sadhanala, A.; Briane, A.; Halpert, J. E.; Broch, K.; Hodgkiss, J. M.; Friend, R. H.; Deschler, F. Hot-carrier cooling and photoinduced refractive index changes in organic−inorganic lead halide perovskites. *Nat. Commun.* **2015**, *6*, 8420.

(59) Wang, L.; Wang, H.; Nughays, R.; Ogieglo, W.; Yin, J.; Gutierrez-Arzaluz, L.; Zhang, X.; Wang, J.-X.; Pinnau, I.; Bakr, O. M.; Mohammed, O. F. Phonon-driven transient bandgap renormalization in perovskite single crystals. *Mater. Horiz.* **2023**, *10*, 4192.

(60) Hopper, T. R.; Gorodetsky, A.; Frost, J. M.; Muller, C.; Lovrincic, R.; Bakulin, A. A. Ultrafast Intraband Spectroscopy of Hot-Carrier Cooling in Lead-Halide Perovskites. *ACS Energy Lett.* **2018**, *3*, 2199−2205.

(61) Chen, J.; Messing, M. E.; Zheng, K.; Pullerits, T. Cation-Dependent Hot Carrier Cooling in Halide Perovskite Nanocrystals. *J. Am. Chem. Soc.* **2019**, *141*, 3532−3540.

(62) Hopper, T. R.; Gorodetsky, A.; Jeong, A.; Krieg, F.; Bodnarchuk, M. I.; Maimaris, M.; Chaplain, M.; Macdonald, T. J.; Huang, X.; Lovrincic, R.; Kovalenko, M. V.; Bakulin, A. A. Hot Carrier Dynamics in Perovskite Nanocrystal Solids: Role of the Cold Carriers, Nanoconfinement, and the Surface. *Nano Lett.* **2020**, *20*, 2271−2278.

(63) Chung, H.; Jung, S. I.; Kim, H. J.; Cha, W.; Sim, E.; Kim, D.; Koh, W.-K.; Kim, J. Composition-Dependent Hot Carrier Relaxation Dynamics in Cesium Lead Halide ($CsPbX_3$, X = Br and I) Perovskite Nanocrystals. *Angew. Chem., Int. Ed.* **2017**, *56*, 4160−4164.

(64) Rossi, D.; Wang, H.; Dong, Y.; Qiao, T.; Qian, X.; Son, D. H. Light-Induced Activation of Forbidden Exciton Transition in Strongly Confined Perovskite Quantum Dots. *ACS Nano* **2018**, *12*, 12436−12443.

(65) Makarov, N. S.; Guo, S.; Isaienko, O.; Liu, W.; Robel, I.; Klimov, V. I. Spectral and Dynamical Properties of Single Excitons, Biexcitons, and Trions in C-sium−Lead-Halide Perovskite Quantum Dots. *Nano Lett.* **2016**, *16*, 2349−2362.

(66) Kim, T.; Jung, S. I.; Ham, S.; Chung, H.; Kim, D. Elucidation of Photoluminescence Blinking Mechanism and Multiexciton Dynamics in Hybrid Organic−Inorganic Perovskite Quantum Dots. *Small* **2019**, *15*, 190035.

(67) Sun, Q.; Zhao, C.; Yin, Z.; Wang, S.; Leng, J.; Tian, W.; Jin, S. Ultrafast and High-Yield Polaronic Exciton Dissociation in Two-Dimensional Perovskites. *J. Am. Chem. Soc.* **2021**, *143*, 19128−19136.

(68) Tao, W.; Zhang, Y.; Zhu, H. Dynamic Exciton Polaron in Two-Dimensional Lead Halide Perovskites and Implications for Optoelectronic Applications. *Acc. Chem. Res.* **2022**, *55*, 345−353.

(69) Li, S.; Luo, J.; Liu, J.; Tang, J. Self-Trapped Excitons in All-Inorganic Halide Perovskites: Fundamentals, Status, and Potential Applications. *J. Phys. Chem. Lett.* **2019**, *10*, 1999−2007.

(70) Luo, B.; Liang, D.; Sun, S.; Xiao, Y.; Lian, X.; Li, X.; Li, M.-D.; Huang, X.-C.; Zhang, J. Z. Breaking Forbidden Transitions for Emission of Self-Trapped Excitons in Two Dimensional $(F_2CHCH_2NH_3)_2CdBr_4$ Perovskite through Pb Alloying. *J. Phys. Chem. Lett.* **2020**, *11*, 199−205.

(71) Tran, N. L.; Elkins, M. H.; McMeekin, D. P.; Snaith, H. J.; Scholes, J. D. Observation of Charge Generation via Photoinduced Stark Effect in Mixed-Cation Lead Bromide Perovskite Thin Films. *J. Phys. Chem. Lett.* **2020**, *11*, 10081−10087.

(72) Gelinas, S.; Rao, A.; Kumar, A.; Smith, S. L.; Chin, A. W.; Clark, J.; van der Poll, T. S.; Bazan, G.; Friend, R. H. Ultrafast Long-Range Charge Separation in Organic Semiconductor Photovoltaic Diodes. *Science* **2014**, *343*, 512−516.

(73) Li, Y.; He, S.; Luo, X.; Lu, X.; Wu, K. Strong Spin-Selective Optical Stark Effect in Lead Halide Perovskite Quantum Dots. *J. Phys. Chem. Lett.* **2020**, *11*, 3594−3600.

(74) Shrivastava, M.; Krieg, F.; Mandal, D.; Poonia, A. K.; Bera, S. K.; Kovalenko, M. V.; Adarsh, K. V. Room-Temperature Anomalous Coherent Excitonic Optical Stark Effect in Metal Halide Perovskite Quantum Dots. *Nano Lett.* **2022**, *22*, 808−814.

(75) Walters, G.; Wei, M.; Voznyy, O.; Quintero-Bermudez, R.; Kiani, A.; Smilgies, D.-M.; Munir, R.; Amassian, A.; Hoogland, S.; Sargent, E. The quantum-confined Stark effect in layered hybrid perovskites mediated by orientational polarizability of confined dipoles. *Nat. Commun.* **2018**, *9*, 4214.

(76) Fish, G. C.; Terpstra, A. T.; Ducinskas, A.; Almalki, M.; Carbone, L. C.; Pfeifer, L.; Gratzel, M.; Moser, J.-E.; Milic, J. V. The Impact of Spacer Size on Charge Transfer Excitons in Dion−Jacobson and Ruddlesden−Popper Layered Hybrid Perovskites. *J. Phys. Chem. Lett.* **2023**, *14*, 6248−6254.

(77) Ziffer, M. E.; Mohammed, J. C.; Ginger, D. S. Electroabsorption Spectroscopy Measurements of the Exciton Binding Energy, Electron−Hole Reduced Effective Mass, and Band Gap in the Perovskite $CH_3NH_3PbI_3$. *ACS Photonics* **2016**, *3*, 1060−1068.

(78) Meggiolaro, D.; Ambrosio, F.; Mosconi, E.; Mahata, A.; De Angelis, F. Polarons in Metal Halide Perovskites. *Adv. Energy Mater.* **2020**, *10*, 1902748.

(79) Sung, J.; Schnedermann, C.; Ni, L.; Sadhanala, A.; Chen, R. Y. S.; Cho, C.; Priest, L.; Lim, J. M.; Kim, H.-K.; Monserrat, B.; Kukura, P.; Rao, A. Long-range ballistic propagation of carriers in methylammonium lead iodide perovskite thin films. *Nat. Phys.* **2020**, *16*, 171−176.

(80) Crisp, R. W.; Schrauben, J. N.; Beard, M. C.; Luther, J. M.; Johnson, J. C. Coherent Exciton Delocalization in Strongly Coupled Quantum Dot Arrays. *Nano Lett.* **2013**, *13*, 4862−4869.

(81) Vickers, E. T.; Graham, T. A.; Chowdhury, A. H.; Bahrami, B.; Dreskin, B.; Lindley, S.; Naghadeh, S. B.; Qiao, Q.; Zhang, J. Z. Improving Charge Carrier Delocalization in Perovskite Quantum Dots by Surface Passivation with Conductive Aromatic Ligands. *ACS Energy Lett.* **2018**, *3*, 2931−2939.

(82) Frost, J. M.; Whalley, L. D.; Walsh, A. Slow Cooling of Hot Polarons in Halide Perovskite Solar Cells. *ACS Energy Lett.* **2017**, *2*, 2647−2652.

(83) Yang, J.; Wen, X.; Xia, H.; Sheng, R.; Ma, Q.; Kim, J.; Tapping, P.; Harada, T.; Kee, T. W.; Huang, F.; Cheng, Y.-B.; Green, M.; Ho-Baillie, A.; Huang, S.; Shrestha, S.; Patterson, R.; Conibeer, G. Acoustic-optical phonon up-conversion and hot-phonon bottleneck in lead-halide perovskites. *Nat. Commun.* **2017**, *8*, 14120.

(84) Fu, J.; Xu, Q.; Han, G.; Wu, B.; Huan, C. H. A.; Leek, M. L.; Sum, T. C. Hot carrier cooling mechanisms in halide perovskites. *Nat. Commun.* **2017**, *8*, 1300.

(85) Zhu, H.; Miyata, K.; Fu, Y.; Wang, J.; Joshi, P. P.; Niesner, D.; Williams, K. W.; Jin, S.; Zhu, X.-Y. Screening in crystalline liquids protects energetic carriers in hybrid perovskites. *Science* **2016**, *353*, 1409−1413.

(86) Li, M.; Bhaumik, S.; Goh, T. W.; Kumar, M. S.; Yantara, N.; Gratzel, M.; Mhaisalkar, S.; Mathews, N.; Sum, T. C. Slow cooling and highly efficient extraction of hot carriers in colloidal perovskite nanocrystals. *Nat. Commun.* **2017**, *8*, 14350.

(87) Manser, J. S.; Kamat, P. V. Band filling with free charge carriers in organometal halide perovskites. *Nat. Photonics* **2014**, *8*, 737−743.